Skarn formation between metachalk and agglomerate in the Central Ring Complex, Isle of Arran, Scotland

G. CRESSEY

Department of Mineralogy, British Museum (Natural History), Cromwell Road, London, SW7 5BD

Abstract

A skarn mineral assemblage occurs at the junction between vent pyroclastics and a xenolithic Cretaceous chalk block which subsided into the collapsed caldera of the Central Ring Complex, Isle of Arran, Scotland. Adjacent to the metachalk marble an andradite garnet exoskarn zone has developed at the expense of the carbonate. An andradite–grossular/diopsidic clinopyroxene endoskarn zone has formed in the surrounding agglomerate, and a magnetite exoskarn is present in places between the andradite and garnet/pyroxene zones. The andraditic exoskarn garnets have fluor-hydrogarnet components, indicating that fluorine was present in the metasomatic fluid. From petrographic evidence, three distinct episodes of exoskarn garnet crystallization can be recognized, in which the fluor-hydrogarnet component steadily increased as a function of time, which probably reflects falling temperature. The *REE* compositions of the exoskarn minerals are regarded as having been largely inherited from the carbonate, and the exoskarn garnets increasingly fractionated *HREE* with time. The endoskarn and agglomerate have also been epidotized. The *REE* signatures of epidotes appear to be inherited partially from precursor clinopyroxenes or feldspars, which have been replaced by epidote. Late-stage vein minerals include prehnite, laumontite and K-rich laumontite, and their *REE* compositions appear to have been derived from the marble, probably via *REE* fluoro-complexes in the fluid.

KEYWORDS: skarn mineralogy, fluor-hydrogarnets, rare earth elements, chalk xenolith, pyroclastics, Isle of Arran, Scotland.

Introduction

THE Central Ring Complex of Arran (Tyrrell, 1928; King, 1955) represents the caldera of a Tertiary volcanic centre. This igneous mass has a near-circular outcrop pattern about 5 km across and consists predominantly of granites and acid pyroclastic agglomerates in approximately concentric outcrop relationships, a pattern which may owe its origin to late ring-dyke formation. However, a detailed petrogenetic interpretation of this centre is extremely complex (King, 1954, 1955) owing to its extensive multi-event volcanic history involving a wide spectrum of igneous rock types, their late mobilization, corrosion and brecciation by fluids, and the metamorphic and metasomatic effects of late felsic intrusions. Blocks of displaced Mesozoic sedimentary rocks incorporated in the volcanic agglomerates were first described by Gunn (1903), who recognized xenoliths of Triassic, Jurassic and Cretaceous rocks by their lithologies and fossil contents. These sediments and basalt plateau lavas within the complex are regarded by King (1955) as remnants of the original cover, through which the Tertiary volcano erupted, and which subsequently subsided into the collapsed caldera. Caldera subsidence of the order of 1 km has been suggested by King (1955) based on an estimate of the thickness of the pre-caldera stratigraphic succession now removed by erosion. A large xenolithic block of Cretaceous chalk surrounded by agglomerate occurs at Creag an Fheidh, 400 m south of the road bridge at Glenloig. The chalk has been metamorphosed to marble. The existence of a skarn mineral assemblage between the metachalk and vent pyroclastics at this locality was communicated by the author to Drs W. S. McKerrow and F. B. Atkins in order that they might include information concerning this occurrence in their field guide to the Isle of Arran (1985). The present work is concerned with the mineralogical and geochemical aspects of this previously unreported skarn.

Mineralogical Magazine, June 1987, Vol. 51, pp. 231–46

Field occurrence and petrography

The xenolithic metachalk block at Creag an Fheidh is situated in a steeply sloping hollow 15 to 20 m wide running north–south and bounded on either side by crags of agglomerate. Presumably this hollow has formed mainly as a result of carbonate dissolution, but past quarrying (for local agricultural use) is partly responsible for the erosion and a cave some 12 m long has been excavated further into the limestone block on the western side of the hollow. The xenolithic block is therefore at least 30 m long in one dimension. The limestone is overlain directly by plateau basalt (King, 1955) which forms the roof of the cave. This basalt may therefore form part of the same xenolithic block. Skarn development at the contact of the limestone and the surrounding agglomerate host is most clearly visible opposite the cave on the eastern side of the hollow.

The chalk has recrystallized to a fine-grained grey marble and its sinuous contact with the skarn is marked by a zone of variable width up to 2 cm of yellowish garnet. This contact is disturbed by numerous small fractures roughly perpendicular to the contact with displacements of up to a few centimetres. The agglomerate in contact with the limestone consists predominantly of basaltic and basaltic tuff fragments which are sub-angular to rounded in shape and represent a wide variety of textural types. The zone of skarn development in the agglomerate is variable in width, but averages 10 cm and consists of a greenish brown fine-grained intergrowth of garnet, clinopyroxene and epidote in which altered agglomerate rock fragments can still be discerned. Several metres beyond the skarn zone and adjacent basaltic vent agglomerate the pyroclastics become more felsic in character and contain angular to rounded fragments (up to several centimetres in size) of altered basalt, andesite, felsite, vein quartz, sandstone (?Permian) and schist (?Dalradian). Much of the fine-grained material is chloritic and probably represents comminuted particles of basaltic material. The groundmass is largely rhyolitic and is vesicular in places. Epidote, calcite and chlorite are abundant in the agglomerate and suggest a complex history of post-caldera hydrothermal activity. The induration and epidotization of the pyroclastics is, in this respect, similar to the propylitization effects described by Walker (1971) around the volcanic ring complex in Mull.

A schematic representation of the skarn zonation is shown in Fig. 1. The marble is composed of a microcrystalline mosaic of calcite grains generally 50 to 100 μm in size. However, a coarser texture of millimetre-sized single crystals is frequently developed immediately adjacent to the garnet skarn and in vein networks near to the skarn contact. Where the andradite garnet band has suffered brittle fracture and has undergone displacement into the marble along fracture lines roughly perpendicular to the skarn contact, coarse-grained calcite has crystallized in the voids created by such movement. Plastic deformation of twin planes in this coarse-grained calcite indicates that post-crystallization movement occurred along such fractures. The fabric of the fine-grained marble also indicates deformation by plastic flow and recrystallization around these faulted rigid garnet fragments. Veins of very much finer-grained calcite, showing flow structure and containing rounded fragments of fluorapatite, also occur near to the skarn contact.

The exoskarn, developed at the expense of the carbonate, represents the first product of fluid-

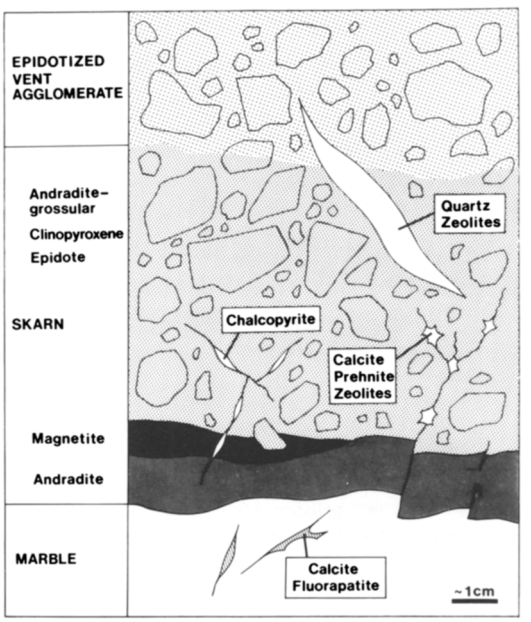

FIG. 1. Schematic representation of the skarn zonation between the metachalk xenolith and vent pyroclastics. The exoskarn, developed at the expense of the limestone, consists of fractured yellow andradite garnet. The endoskarn, developed in the agglomerate, consists of andradite–grossular garnet and clinopyroxene. Both the endoskarn and agglomerate are epidotized; epidote partially replaces clinopyroxene in the endoskarn and pseudomorphs feldspars in rock fragments. A magnetite exoskarn zone is present in places between the andradite exoskarn and the endoskarn. Late-stage fractures and cavities are filled by sulphides, calcite, prehnite and zeolites. Lenses containing euhedral quartz and interstitial zeolites occur in the agglomerate and endoskarn.

calcite metasomatic reaction, and consists almost entirely of massive yellowish andraditic garnet with minor diopsidic clinopyroxene present in places as tiny (10 to 20 μm) inclusions. The garnet is also occasionally clouded by wollastonite needles which, together with the clinopyroxene, may represent the remnant of an earlier-formed reaction zone. Three distinct phases of garnet crystallization, related to fracturing and fluid activity, can be recognized; this is discussed later along with garnet chemistry.

A zone of magnetite sometimes occurs between the andradite exoskarn and the metasomatized agglomerate (endoskarn). The magnetite in this zone appears largely to have replaced the carbonate and can therefore be regarded as an exoskarn mineral. However, agglomerate rock fragments are occasionally present as inclusions within the magnetite on the endoskarn side of the magnetite zone, indicating that some replacement of the agglomerate matrix by magnetite also took place. Magnetite in this zone can therefore also be included in the endoskarn assemblage. Small amounts of magnetite occur throughout the endoskarn, often partially mantling agglomerate rock fragments. The presence of magnetite surrounding single euhedral garnets in the endoskarn indicates that some magnetite crystallization took place after the formation of these garnets. Sulphide minerals associated with the magnetite exoskarn/endoskarn zone include chalcopyrite, sphalerite and pyrite, all of which crystallized later than the magnetite in cavities and fractures in the magnetite and endoskarn.

The endoskarn is very complex in texture and mineralogy because of the variable nature of the precursor agglomerate. In general, metasomatic alteration of the agglomerate has resulted in the development of a fine-grained intimate intergrowth of andradite-grossular garnet and clinopyroxene, mainly in the agglomerate matrix. Both the endoskarn and the agglomerate outside the skarn zone are epidotized. However, this hydrothermal alteration is more extensive in the endoskarn than the agglomerate. In the endoskarn, epidote partially replaces clinopyroxene, but not garnet. In addition epidote pseudomorphically replaces the feldspars and augite in agglomerate rock fragments in which ophitic textures can be still recognised. Most feldspathic rock fragments in the endoskarn are less than about 0.5 cm in diameter and in all these the feldspars have been completely replaced by epidote. Some larger tuffaceous fragments, altered to a mixture of amphibole, chlorite and albite, are not epidotized. Epidote also occurs as single crystals, up to 1 mm long, in cavities.

Thin fractures traverse the endoskarn in various directions; epidote, prehnite, calcite and zeolites form the fracture-fill material. Pale lenses up to 1 cm wide occur in the endoskarn and agglomerate and contain zeolites and calcite interstitial to subhedral and euhedral quartz. Zeolites and prehnite with radiating habit have also crystallized in cavities and represent the later stages of metasomatism.

Comparison with other skarns. The skarn mineralogy described here is characteristic of the Fe class of calcic skarns, reviewed by Einaudi *et al.* (1981) and by Einaudi and Burt (1982). The exoskarn zonation calcite-andradite-magnetite (Fig. 1) and the (now remnant) earlier possible zonation calcite-wollastonite-clinopyroxene-(andradite)-(magnetite) are sequences which are frequently observed in Ca–Fe–Si skarns (see Burt, 1974). Diffusion models are commonly used to explain such zonation sequences, and assume the simultaneous development of zones in response to component chemical potential gradients which develop between juxtaposed dissimilar host rocks (Burt, 1974). In the exoskarn described here, it is clear that andradite has replaced earlier clinopyroxene and several phases of compositionally distinct andraditic garnet growth can be recognised; these phenomena are commonplace in many skarns (e.g. see Shimazaki, 1969; Atkinson *et al.*, 1982; Harris and Einaudi, 1982; Uchida and Iiyama, 1982). The instability of hedenbergitic clinopyroxene relative to andradite is essentially related to an increase in f_{O_2} in the hydrothermal fluid system. Features in common with other skarns also include the presence of epidote in the endoskarn assemblage (e.g. Uchida and Iiyama, 1982; Kitamura, 1975; Shimazaki, 1969), the post-magnetite formation of sulphides (e.g. Uchida and Iiyama, 1982), and the late-stage crystallization of zeolites and prehnite (e.g. Einaudi *et al.*, 1981; Shimazaki, 1969; Shoji, 1975).

Analytical techniques

Mineral analyses were carried out by standard electron microprobe techniques using a Cambridge Instruments Microscan 9 for wavelength-dispersive analysis and a Cambridge Instruments Geoscan with a Link Systems Si(Li) detector for energy-dispersive analysis. Standards were pure elements, oxides and well-characterized silicates.

The H_2O^+ contents of garnet mineral separates were determined by the technique of Din and Jones (1978) using a CHN elemental analyser. Fluorine contents of garnets were determined using an ion-selective electrode following pyrohydrolytic separation. Because of the small amounts of pure garnet separates available, a semi-micro method using about 5 mg of material was employed to determine Fe^{3+}/Fe^{2+} ratios of garnet separates. After dissolution in an equal-volume mixture of HF (40% w/w) and H_2SO_4 (18M) in an oxygen-free

TABLE 1 ACTIVATION ANALYSES OF MINERAL SEPARATES FROM ARRAN SKARN (PPM ELEMENT)

	MARBLE		SKARN											
			Andradite exoskarn zone				Andradite-grossular garnet, clinopyroxene, epidote endoskarn zone							
			Garnets						Epidotes					Fragment in agglomerate
	Calcite	Calcite + Fluor-apatite	G1	G2	G3	Magnetite	Andradite-grossular garnet	Clino-pyroxene + Epidote	replacing Clino-pyroxene	pseudomor-phs after feldspar	crystals from cavities	Laumontite + Quartz	Prehnite	Amphibole + Chlorite
Source specimen no.	AR531	AR531	AR540	AR540	AR540	AR531	AR531	AR524	AR524	AR531	AR524	AR524	AR540	AR531
Activation analysis no.	1118	1089	8309	8310	8312	1088	1086	8317	8315	1083	8314	8318	8313	1080
Sc	1.1	1.0	0.64	0.9	9.6	10	15	11.9	14.1	15	25.6	2.77	1.47	47
Cr	5	8	23.3	7.8	68.7	178	169	82	160	340	82	19.8	14	1280
Co	3	3.1	6.4	8.3	43.7	169	26	50.6	17.1	35	11.5	18.4	25.6	68
Ni	<10	8	<35	<30	<35	<150	75	125	<35	115	<40	55	<40	<200
Zn	19	21	186	97	486	110	49	697	65	65	41	962	287	100
Hf	<0.1	<0.2	<0.15	<0.1	1.42	<1	2.5	5.2	3.8	1.7	6.1	0.57	0.55	3
Ta	<0.1	<0.2	<0.05	<0.05	0.15	<0.8	0.5	0.61	0.48	<0.2	0.36	8.3	0.1	<0.7
Rb	<10	<10	<7	<7	<6	<40	<10	<6	<6	<10	<6	12	<8	-
Cs	<0.1	-	<0.3	<0.25	<0.25	-	-	1.25	<0.25	-	<0.25	7	<0.3	-
Sb	1.3	0.4	0.27	0.31	0.87	3.6	1.8	2.9	2.7	4.6	8.3	1.1	1.28	1
Th	0.5	0.4	0.25	0.37	1.1	1.4	5.9	5	5	3	1.2	0.95	1	2.6
U	1	3	0.4	0.52	0.45	2	1.1	1.7	2.2	1.5	1.3	0.7	0.5	0.6
La	15.5	38.2	4.2	5.3	7.2	28.2	13.3	24.9	34.5	21.4	22.9	19.8	12.3	8.7
Ce	11.5	27.2	5	5.4	7.4	24.3	27.8	37.9	50.5	39	42.6	13.7	12.5	17.8
Nd	11.1	31	4.6	7	7.3	20	15.1	23.9	30.7	21.6	26.2	14.6	6.2	9.1
Sm	1.96	6.2	0.91	1.49	2.27	3.5	3.2	5.05	6.5	4.4	6.12	2.49	1.25	2.9
Eu	0.54	1.51	0.32	0.41	0.5	1.12	1.02	1.09	1.59	2	1.94	0.39	0.27	0.8
Gd	-	-	0.9	1.6	3.3	-	-	4.8	5.9	4.4	5.9	2.4	<1.5	-
Tb	0.35	1.15	0.14	0.25	0.62	0.66	0.63	0.79	0.97	0.75	1.05	0.39	0.17	0.6
Ho	-	1.3	<0.2	0.3	0.82	-	0.8	0.9	1.3	0.8	1.7	0.4	<0.5	-
Tm	-	0.33	-	-	-	-	0.31	0.41	0.48	0.25	0.65	0.14	<0.1	0.3
Yb	0.78	2.2	0.3	0.79	2.33	1.2	2.1	3.02	3.62	1.7	4.35	1.04	0.51	2.4
Lu	0.1	0.16	0.04	0.13	0.35	0.11	0.3	0.41	0.48	0.23	0.63	0.13	0.09	0.34
$(Ce/Ce^*)_{CN}$	0.35	0.33	0.52	0.42	0.45	0.41	0.90	0.68	0.66	0.81	0.80	0.32	0.50	0.90
$(Eu/Eu^*)_{CN}$	0.81	0.70	1.08	0.82	0.56	0.92	0.91	0.67	0.78	1.39	0.98	0.49	0.68	0.77
$(La/Yb)_{CN}$	12.8	11.2	9.08	4.34	2.00	15.2	4.10	5.33	6.17	8.14	3.41	12.30	15.60	2.34

Ce* and Eu* are the chondrite-normalized (CN) linearly interpolated values between La - Nd and Sm - Gd respectively.

nitrogen atmosphere at 100 °C, Fe^{2+} and total Fe (after reduction) were determined colorimetrically using 2,2′bipyridyl. Experiments using this method on standard rock BR resulted in the recovery of 96% of the total Fe quoted by Abbey (1983) and an Fe^{3+}/Fe^{2+} ratio within 3% of the standard rock data. The total iron recovery in garnet samples was also low (around 90% relative to microprobe values) because of problems encountered in dissolving garnet whilst preserving the oxidation state of the parent material. However, the ratio Fe^{3+}/Fe^{2+} is considered to be representative of the whole sample and is estimated to be accurate to ±10–15%. Precision in the determination of Fe^{2+} for these garnets was demonstrated to be within 4% (1 sigma).

Trace elements in mineral separates were determined by instrumental neutron activation analysis (INAA), using high-resolution Ge and Ge(Li) detectors of resolutions 560 eV at 122 keV and 1.8 keV at 1.33 MeV respectively. Rare earth element concentrations were determined by the technique described by Henderson and Williams (1981). Results are shown in Table 1 and chondrite-normalized rare earth concentrations plotted against atomic number are shown in Figs. 4, 6 and 8, using the chondrite values given by Wakita *et al.* (1971). Accuracy and precision of the INAA data are estimated to be 5–10% (1 sigma level). The precision and estimated detection limits, quoted in Table 1, are related to sample weight and matrix effects in individual samples. The USGS standard rock BHVO-1 (basalt) analysed under the same conditions gave results generally within ±5% of the values quoted by Abbey (1983).

Mineral separates for INAA shown in Table 1 were obtained by handpicking, sieving and using a Cook isodynamic magnetic separator. Grains for magnetic separation were from dried sieve fractions between 50 and 150 μm in size. Three andraditic garnet fractions (G1, G2 and G3) of different paramagnetic susceptibilities were successfully separated with increasing current. A pure epidote fraction was magnetically separated from epidote + clinopyroxene mixtures, but a pure clinopyroxene separate could not be obtained. However, gentle grinding and sieving of this epidote + clinopyroxene residue slightly enhanced the proportion of clinopyroxene in the finer-grained fraction. A prehnite + calcite residue was obtained by progressive separation of garnet, epidote and clinopyroxene in several stages of increasing current. The calcite was removed by dissolution in weak HCl, leaving only prehnite in the final sample. A quartz + zeolite residue was obtained after the magnetic separation of small amounts of garnet, clinopyroxene and epidote. Gentle crushing and sieving of this residue through progressively finer mesh greatly enhanced laumontite in the smallest grain size fraction. Heavy liquid separation was not used in order to avoid any trace element contamination. Source material for INAA (handpicked grains and material for magnetic separations) were taken from polished slices, and corresponding microprobe analyses were carried out on adjacent serial sections and/or polished grain mounts of separated material. The efficacy of magnetic separations was continually monitored by X-ray powder diffractometry. Cell edges of garnets in final separates G1, G2 and G3 were also measured from film (114.6 mm diameter camera) and extrapolation to 90° θ was made using a Nelson–Riley function.

All analytical procedures were carried out in the Department of Mineralogy, British Museum (Natural History).

Andradite exoskarn zone: mineralogy and petrogenesis

The exoskarn consists almost entirely of massive yellowish andraditic garnet which varies irregularly in hand specimen from dark yellow, through yellow-green to brown, and pale, fine-grained garnet fills a network of fine fractures. In thin section three distinct garnet types can be recognized and have been designated G1, G2 and G3. G1 is dark yellow and isotropic, G2 is pale yellow and isotropic, and G3 is colourless to brownish and anisotropic. The petrogenetic relationships between these three episodes of garnet crystallization are illustrated in Figs. 2 and 3. G1 was the earliest to crystallize and is sometimes clouded by a myriad of 10–20 μm diopsidic clinopyroxene inclusions. Formation of garnets G2 and G3 involved two separate phases of fracturing followed by metasomatic fluid activity along fracture pathways. The early fracturing (phase 1) has affected only garnet G1, and garnet G2 has formed at the expense of G1 and extends into G1 from these fracture surfaces, suggesting that a process of wall-rock alteration by fluids was operative. Boundaries between the yellow G1 and the paler G2 are abrupt and are near-parallel to adjacent fractures. The islands of G1 remaining

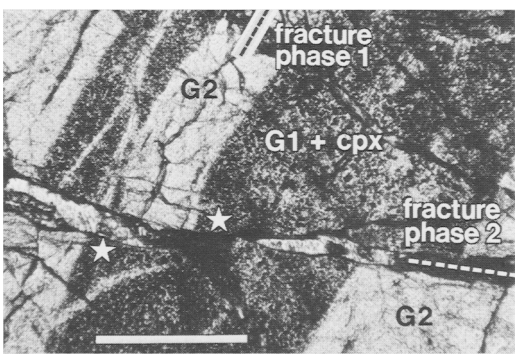

FIG. 2. Petrogenetic relationship between exoskarn garnets G1 and G2. Transmitted light. Wall-rock alteration of G1 by fluids along fracture pathways (fracture phase 1) has also resulted in the removal of clinopyroxene (cpx) inclusions during the recrystallization of garnet G1 to garnet G2. Later fracturing (phase 2) affects both G1 and G2 (relative movement indicated by star symbols). Line of fracture phase 2 extends into a brecciated area similar to that shown in Fig. 3. Scale bar 0.5 mm.

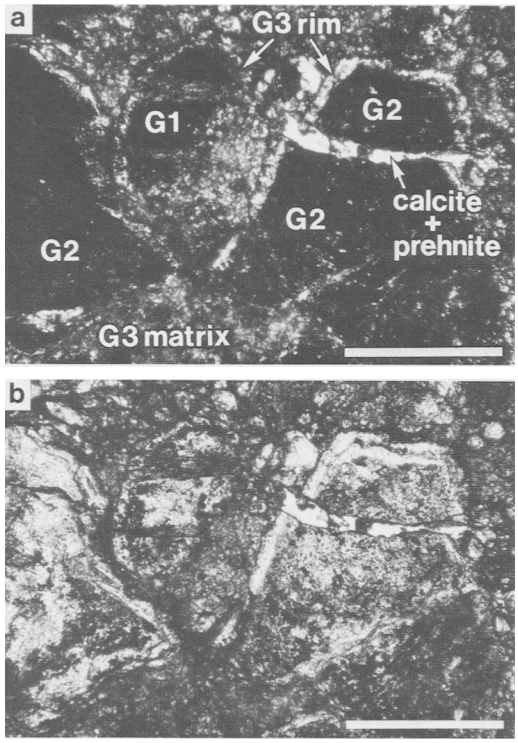

FIG. 3. Petrogenetic relationships between exoskarn garnet phase G3 (anisotropic) and earlier exoskarn garnets G1 (dark yellow, isotropic) and G2 (pale yellow, isotropic). Garnet G3 forms zoned overgrowth rims on brecciated fragments of earlier garnets. G3 also forms the fault breccia matrix. (*a*) Transmitted light, crossed polars; (*b*) plane polarized light. Scale bar 0.5 mm.

reflect the phase 1 fracture network pattern. In addition, clinopyroxene inclusions are completely absent in G2, enabling the abrupt boundary between G1 (where it contains clinopyroxene inclusions) and G2 (which crystallized at the expense of G1 + clinopyroxene) to be seen clearly (Fig. 2). The second and later phase of fracturing affects both G1 and G2 and is also accompanied by micro-faulting (Fig. 2) and brecciation of the G1 and G2 garnet phases (Fig. 3). The third garnet phase, G3, forms anisotropic overgrowth rims, up to 50 μm thick, on the brecciated fragments of G1 and G2. Garnet G3 also forms a fine-grained matrix to this fault breccia. Calcite and prehnite crystallized within cracks produced during fracture phase 2 and later (see Fig. 3).

The exoskarn consists of approximately 10% G1, 60% G2 and 30% G3 by volume. The paramagnetic susceptibilities of these three garnet phases (susceptibility G1 > G2 > G3) are sufficiently different to allow them to be separated successfully by the isodynamic magnetic method. The purity of final separates was checked by X-ray powder diffractometry: G1 and G2 fractions contained only a trace (< 1 wt. %) of calcite, and G3 contained only a trace of calcite and clinopyroxene. The residue from the magnetic separation contained clinopyroxene, calcite, epidote, grossular-rich garnet and prehnite.

Garnet chemistry. Microprobe analyses of grain mount samples G1, G2 and G3 magnetic separates are given in Table 2. For microprobe analysis garnet grains were mounted in a thin film of epoxy resin on glass, and polished down to a thickness which enabled their characteristics in transmitted light and their chemistries to be compared with those of analysed garnets in polished thin section in which the spatial relationships between garnets had been preserved. In this way the magnetic fractions were confirmed to be those designated G1, G2 and G3 from optical thin section examination. Samples of grains G1, G2 and G3 were mounted on the same glass slide and microprobe analyses of each were performed in rotation under the same operating conditions in order to detect small average differences in composition. H_2O^+, F and Fe^{3+}/Fe^{2+} destructive determinations were carried out on samples after their analysis by INAA.

Garnets G1, G2 and G3 can be described as fluor-hydrogarnets (see Table 2), and show a trend of steadily increasing H_2O and F content from G1 to G3. This may simply reflect an evolving trend in the metasomatic fluid composition, but it may also involve a complex interplay between garnet crystal chemistry and changing physicochemical conditions. Fe^{3+}/Fe^{2+} ratios determined for G1 and G2 are taken to be identical (within measurement error), but Fe^{3+}/Fe^{2+} determined for G3 shows a five-fold decrease, indicating a trend to more reducing conditions with time. Garnet compositions (Table 2) are presented as cation numbers per 12(O, OH, F). Fe^{2+} has first been assigned to 8-coordinate sites with all other divalent cation types to total 3.000, then the remaining Fe^{2+} has been assigned to octahedral sites with Fe^{3+} and Al^{3+}. The Al^{3+} remaining, after summation of octahedral cations to 2.000, has been assigned to tetrahedral sites. The substitution of Fe^{2+} for Fe^{3+} in octahedral sites, and the presence of tetrahedral (Si,Al) vacancies, is required in order to explain satisfactorily the substitution of OH^- and F^- for O^{2-}, assuming that the anion framework structure of garnet is preserved. An additional indication that the assumption of octahedral Fe^{2+} is reasonable is provided by the comparison of measured and calculated unit cell edges (see Table 2), using the

TABLE 2. CHEMISTRY OF GARNETS FROM ANDRADITE EXOSKARN ZONE

		Energy dispersive microprobe analysis at 15 kV					
	Source specimin no.	AR540: magnetically separated garnet grains, paramagnetic susceptibility G1>G2>G3.					
		G1		G2		G3	
	colour	dark yellow		pale yellow-green		brownish	
	optics	isotropic		isotropic		anisotropic	
	genesis	early		intermediate		late	
	n=number of analyses	mean n=35	std. dev.	mean. n=49	std. dev.	mean n=32	std. dev.
	Fe (element)	22.10	(0.45)	22.15	(0.44)	13.36	(2.04)
(1)	Fe^{3+}/Fe^{2+}	44.3		43.5		9.2	
	SiO_2	35.17	(0.37)	35.46	(0.42)	35.73	(0.50)
	Al_2O_3	0.16	(0.30)	0.23	(0.38)	8.88	(1.98)
	TiO_2	n.d.		n.d.		0.50	(0.40)
	Cr_2O_3	n.d.		n.d.		n.d.	
(1)	Fe_2O_3	30.90		30.96		17.23	
(1)	FeO	0.63		0.64		1.68	
	MgO	n.d.		n.d.		n.d.	
	MnO	0.11	(0.17)	0.08	(0.15)	0.47	(0.12)
	CaO	32.88	(0.55)	32.69	(0.40)	34.31	(0.40)
(2)	H_2O	0.21		0.45		0.90	
(3)	F	0.12		0.17		0.25	
(4)	Cl	n.d.		n.d.		n.d.	
	O≡F	0.05		0.07		0.11	
	total	100.13		100.61		99.84	
		cations per 12 (O, OH, F)					
	Si	2.967	2.969	2.962		2.872	2.884
	Al^{IV}	0.002		-		0.012	
	Al^{VI}	0.014	2.000	0.022	1.986	0.829	2.000
	Ti	-		-		0.030	
	Fe^{3+}	1.962		1.946		1.042	
	$Fe^{2+}VI$	0.024		*0.018		0.099	
	Fe^{2+}	0.021	3.000	*0.027	2.958	0.014	3.000
	Mn	0.008		0.006		0.032	
	Ca	2.971		2.925		2.954	
	OH	0.118	0.150	0.251	0.296	0.482	0.545
	F	0.032		0.045		0.063	
(5)	$X_{Fe3+}(VI)$	0.98		0.98		0.52	
(6)	$X_{Fe2+}(VI)$	0.01		0.01		0.05	
(7)	Σapparent cation vacancies	0.4%		1.2%		1.5%	
(8)	cell edge (measured)	12.059	(0.001)	12.058	(0.001)	11.95-11.97	
(9)	cell edge (calc.)	12.060		12.058		11.962	
	activation analysis no.	8309		8310		8312	

n.d. = not detected by microprobe analysis.
(1) Fe^{3+}/Fe^{2+} determined colorimetrically, after acid dissolution. Fe_2O_3 and FeO calculated from microprobe Fe (element) total and Fe^{3+}/Fe^{2+} values.
(2) H_2O determined using CHN analyser.
(3) F determined by solution chemistry.
(4) Cl levels investigated by wavelength dispersive analysis at 20 kV.
(5) $X_{Fe3+}(VI) = Fe^{3+}/\Sigma$ octahedrally assigned cations.
(6) $X_{Fe2+}(VI) = Fe^{2+}(VI)/\Sigma$ octahedrally assigned cations.
(7) Deficiencies relative to 100% maximum of 8 cations, and assuming a garnet anion framework structure of 12 anions per 8 cations.
(8) cell edge by X-ray powder diffraction, 114.6mm diam. camera, extrapolation to 90° θ using Nelson-Riley function.
(9) cell edge calculated from $a = 9.04 + 1.61\langle X\rangle + 1.89\langle Y\rangle$, where $\langle X\rangle$ = mean radius 8-coordinate, and $\langle Y\rangle$ = mean radius 6-coordinate cations (Novak & Gibbs, 1971).
* Fe^{2+} assigned to 8- and 6-coordinate sites on basis of measured cell edge and evaluation of equation in (9).

equation given by Novak and Gibbs (1971) for cell edge calculation from cation radii. Because the amount of Fe^{2+} present in these garnets is small, a variation in Fe^{3+}/Fe^{2+} ratio of up to $\pm 20\%$ has little effect on the calculated proportion of Fe^{2+} and other cations, and the charge-balancing principle discussed above still holds.

G1 and G2 have compositions close to andradite ($X_{Fe^{3+}}(VI) = 0.98$), but G3 shows appreciable Al^{3+} substitution for Fe^{3+} ($X_{Fe^{3+}}(VI) = 0.44$–0.60) and is usually zoned. G3 is also characterized by the presence of Ti and an increase in Mn relative to the earlier garnets. Since the later garnets (G3) are much richer in grossular component, it seems reasonable to assume that the chemical potential ratio μ_{Al}/μ_{Fe} increased with time. However, fluctuations in this ratio may have been responsible for compositional zoning: G3 rim overgrowths on earlier brecciated garnets often show gradual zonation from about 6.5 wt. % Al_2O_3 (inner rim) to 9 wt. % Al_2O_3 (centre rim) to 6 wt. % Al_2O_3 (outer rim). A similar variation in Al_2O_3 content also occurs in the matrix G3 phase. A histogram of $\%Al_2O_3$ plotted against number of analyses for the G3 separate showed an approximately symmetrical Gaussian distribution, with a mean Al_2O_3 value of 8.88% and a standard deviation of 1.98 (see Table 2). However, 53% of analyses are within $\pm 1\%$ of this mean value and taken separately give a mean and standard deviation of 8.86 $\pm 0.58\%$ Al_2O_3. The measured cell edge range (Table 2) also reflects this variation.

The petrogenetic relationship between garnet phases G1 and G2 is distinctly different from that which exists between G3 and the earlier garnets. G3 simply crystallized in voids from a circulating fluid. However, G2 appears to have formed by the recrystallization of G1 involving a process of wall-rock alteration by fluids. The major-element compositions of G1 and G2 are almost identical apart from the slightly higher H_2O and F contents of G2. Deficiencies in calculated cation numbers in 4-, 6- and 8-coordinate sites in G2 indicate that the increased substitution of OH^- and F^- for O^{2-} in G2 may have been accompanied by tetrahedral, octahedral and 8-coordinate cation losses together with some Fe^{2+} substitution for Fe^{3+} in octahedral sites. This suggests a mechanism of transformation from G1 to G2 by fluid diffusion through the oxyanion garnet framework and its modification, by addition of H^+ and substitution by F^-, without total dissolution breakdown. The constancy of andraditic composition may be due to the lack of Al, Mn and Ti in this fluid. Alternatively such elements may be energetically more stable in the fluid phase for the given physicochemical conditions. It is evident that the Mg-rich clinopyroxene inclusions in G1 (see Fig. 2) became unstable in the presence of the fluid during the transformation of G1 to G2, and since Mg is below the microprobe detection limit in these garnets it is likely that Mg was strongly partitioned into the fluid phase and thus removed from the exoskarn during recrystallization of G1 to G2.

From the compositions of these hydrothermal garnets, it is apparent that the metasomatic fluid must have contained water and fluorine. Chlorine was below the microprobe detection limit (about 0.01 wt. %) in all garnets analysed, but this does not necessarily imply the absence of chlorine in the fluid. From ionic size considerations Cl^- is much less likely to be accommodated in the garnet structure than F^- or OH^-. Both meteoric water and magmatic volatile components are considered to have contributed to the fluid phase within the caldera system. HCl, HF, H_2S, CO_2 and SO_2 gases of magmatic origin are likely to have dissolved in circulating groundwaters and may have facilitated the localized leaching of Fe and other elements from caldera rock debris (see Williams and McBirney, 1979, p. 332; Sigurdsson, 1977). The contribution of CO_2 to the fluid is uncertain. Gordon and Greenwood (1971) and Taylor and Liou (1978), however, have shown experimentally that below 400–500 °C the hydrothermal stability of andradite is restricted to water-rich fluids relatively free from CO_2 ($X_{CO_2} < 0.2$). Gustafson (1974) and Shoji (1974) have both shown experimentally that in the system Ca-Fe-Si-O-H andradite develops an increasing hydrogarnet component with decreasing temperature below about 550 °C. It is likely, therefore, that the exoskarn fluor-hydrogarnets may have formed below 550 °C, and that the trend of increasing fluor-hydrogarnet component with time is related to falling temperature. Based on the hydrothermal experiments of Greenwood (1967), wollastonite is stable relative to calcite and quartz in the presence of H_2O–CO_2 fluids with high mole fractions of H_2O component above 400–500 °C at pressures up to 1 kbar. Since remnant wollastonite is present within some of the exoskarn garnets it is likely that these temperatures were achieved. In order to place constraints on the maximum temperature of contact between the chalk and agglomerate, it is necessary to take into account the fast-cooled nature of the rhyolitic matrix from a maximum liquidus temperature around 700 °C, its massive dilution with relatively cold rock debris, the non-welded nature of the agglomerate, and the absence of any magmatic contact or veining of the chalk by rhyolite. It is therefore likely that initial chalk–agglomerate contact temperatures were below 500–600 °C, and the metamorphism and metasomatism of the chalk

within the caldera collapse episode is estimated to have taken place mainly at temperatures below 400–500 °C.

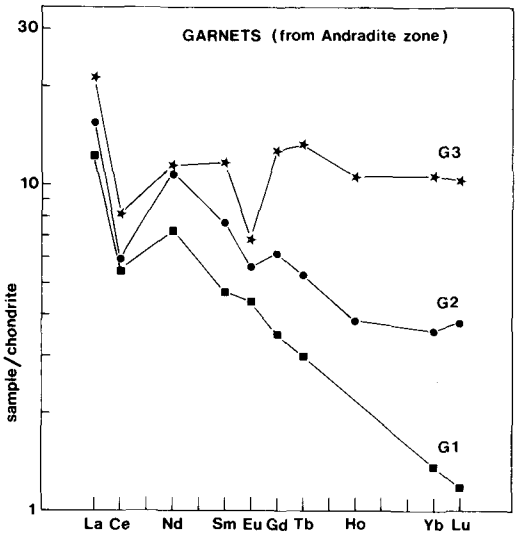

FIG. 4. Chondrite-normalized rare earth concentrations in garnet separates from the andradite exoskarn zone. The petrogenetic garnet sequence G1–G2–G3 indicates a trend towards increased *HREE* uptake with time. Data by INAA.

Garnet trace element data. Trace element concentrations determined by INAA for the magnetically separated garnet fractions G1, G2 and G3 are given in Table 1, and their chondrite-normalized rare earth concentrations are shown in Fig. 4. All trace elements investigated have higher concentrations in garnet G3 than in the earlier formed garnets G1 and G2, with the exception of U, which remains about constant. Concentrations of Sc, Co, Sb, Th and the rare earth elements all show a continual increase in the petrogenetic garnet sequence G1–G2–G3. However, Cr and Zn show a marked decrease in concentration from G1 to G2 (followed by a strong increase in concentration in G3). The decrease could be related to the G1 to G2 transformation energetics resulting in the preferential release of Cr and Zn into the fluid as G1 is modified to G2 by the fluid diffusion, leaching and recrystallization mechanism discussed above. The chondrite-normalized rare earth signatures of garnets G1, G2 and G3 are clearly distinct (Fig. 4), and show a steady increase in all rare earth element concentrations from G1 to G3. G1 shows a light rare earth element (*LREE*) enrichment with a chondrite-normalized ratio $(La/Yb)_{CN} = 9.08$. A change towards increased heavy rare earth element (*HREE*) uptake is clearly evident in G2, $(La/Yb)_{CN} = 4.34$, and in G3, $(La/Yb)_{CN} = 2.0$. G3 has approximately equal chondrite-normalized concentrations of *LREE* and *HREE*.

It is well known that most trace element partition coefficients between crystal and melt/fluid are highly dependent on temperature, pressure and bulk composition. In a review of trace element partitioning behaviour, Irving (1978) presented data which indicate that in garnet–silicate liquid systems, garnet/liquid *REE* distribution coefficients generally increase with decreasing temperature, and that garnet *HREE* fractionation increases with falling temperature. However, because of the interdependence of temperature, pressure and composition, a simple interpretation involving temperature and element distribution is not always possible. Irving and Frey (1978) and Apted and Boettcher (1981) have shown that changes in major element composition in the garnet or silicate liquid can also markedly effect trace element partitioning. The trend of steadily increasing fluor-hydrogarnet component in the exoskarn garnets with time probably indicates formation at progressively lower temperatures. Falling temperature may therefore be responsible for the general trend of increased trace element uptake and the trend towards increased *HREE* fractionation in the sequence G1 to G2 to G3. However, G3 is also characterized by higher Al, Mn and Ti concentrations than the earlier garnets and this major-element compositional change in the garnet (and fluid) is also likely to affect trace element partitioning. Since the trend in increased trace element uptake and the trend towards *HREE* fractionation is more marked in G3 relative to that between G1 and G2 (which have similar major element compositions) it is possible that the trace element partitioning in G3 is more importantly a function of composition rather than simply a function of falling temperature.

The absence of *HREE* enrichment in these garnets of metasomatic origin is in complete contrast to the strong *HREE* fractionation trend generally shown by garnets from metamorphic and igneous parageneses (e.g. Pride and Muecke, 1981; Schnetzler and Philpotts, 1970). The chondrite-normalized *LREE* enrichment and negative Ce anomalies, $(Ce/Ce^*)_{CN} < 1$, shown by the exoskarn minerals (garnet, magnetite, fluorapatite) may be related to the *REE* characteristics of the carbonate (now marble) which the exoskarn minerals have replaced (see Figs. 4 and 8). Calcareous planktonic organisms are known to concentrate *REE* from seawater and have negative Ce anomalies as a result of the ease of oxidation of Ce^{3+} to Ce^{4+} in

the oceans and the subsequent depletion of Ce in seawater by the probable precipitation of CeO_2 (see Fleet, 1984). It is likely, therefore, that the negative Ce anomaly in the marble originated in the biogenic chalk, and that this relative depletion in Ce remained during its recrystallization to marble. It is probable that the exoskarn minerals have inherited much of their *REE* and relative Ce depletion characteristics from the carbonate during its replacement. The chondrite-normalized *REE* patterns of garnet G1, magnetite, fluorapatite and calcite (marble) have very similar slopes and, apart from different Eu anomalies, the only variation that occurs to any extent is in their absolute *REE* contents. This suggests that during exoskarn mineral formation an initial redistribution of the *REE* originally contained in the carbonate took place without appreciable fractionation of the different rare earth elements (except Eu), i.e. local mobilization of *REE* may have taken place. A higher proportion of *REE* was partitioned into the fluorapatite and magnetite relative to garnet. With time, and under more favourable physicochemical conditions (including lower temperatures and bulk composition changes discussed above), *REE* redistribution appears to have taken place and the effective fractionation of *HREE* by garnets G2 and G3 is clearly evident. Another factor which may have influenced the *REE* redistribution could have been the presence of fluorine in the fluid phase. From thermodynamic considerations, Alderton *et al.* (1980) have shown that the *REE* are likely to form stable MF^{2+} and MF_2^+ species in F-rich fluids and can therefore be considered as potentially mobile elements. Additionally the *LREE* fluoro-complexes are possibly more easily formed than those of the *HREE*.

The different Eu anomalies in the exoskarn minerals are presumably related to the presence of Eu^{2+} and Eu^{3+} during the prevailing fluid redox conditions and crystal chemical controls affecting the relative uptake of Eu^{2+} and Eu^{3+}. Garnet G3 exhibits a strong negative Eu anomaly, $(Eu/Eu^*)_{CN} = 0.56$. Preferential partitioning into the garnet structure of Eu^{3+} relative to Eu^{2+} may account for the negative anomalies in garnet, and their magnitudes may reflect changing oxygen fugacities. The development of a slight negative Eu anomaly in G2 and a stronger negative Eu anomaly in G3 suggests that a reduction in f_{O_2} resulted in an increase in the Eu^{2+}/Eu^{3+} ratio in the fluid with time. Corroborative evidence indicating a decrease in f_{O_2} with time is also provided by the decrease in Fe^{3+}/Fe^{2+} measured for garnet G3 relative to the earlier garnets (see Table 2).

Redistribution of other trace elements between exoskarn minerals may also have taken place, and the presence of fluorine in the fluid may have contributed to an increase in the mobilities of elements such as Sc, Cr, Co, Ni and Zn (see Alderton *et al.*, 1980). These elements may also have been introduced into the exoskarn as OH- and F-complexes in the fluid phase with Si, Fe and Al.

Endoskarn mineralogy

The endoskarn consists predominantly of a fine-grained intergrowth of andradite–grossular garnet and diopside–hedenbergite pyroxene which has developed mainly in the matrix around the agglomerate rock fragments. To a large extent the compositions of these metasomatic endoskarn minerals reflect the precursor Si–Al–Fe–Mg chemistry of the original agglomerate. The clinopyroxene (but not the garnet) has been replaced to varying degrees by epidote. Arrested stage alteration of coarse-grained corroded clinopyroxene, showing irregular boundaries against epidote, formed at the expense of the once-euhedral pyroxene, can sometimes be seen optically at high magnifications. Most of the clinopyroxene–garnet intergrowth is very fine-grained, and the replacement of the clinopyroxene by epidote is demonstrated by electron optics and X-ray mapping in Fig. 5. Epidote has pseudomorphically replaced all existing feldspar in the rock fragments, and has also crystallized as large single crystals infilling cavities in the agglomerate. Microprobe analyses of these minerals are shown in Table 3. In general, epidote which has partially replaced diopside–hedenbergite pyroxene is richer in Fe than epidote which has replaced feldspar. Clinopyroxenes richest in the hedenbergite component are often replaced by Fe-rich epidotes in which $M3$ sites are saturated with Fe^{3+}, i.e. $Fe^{3+}/(Fe^{3+}+Al^{3+}) = 0.33$. It is concluded that Fe^{2+} is relatively immobile in this replacement transformation and is accompanied by local oxidation to Fe^{3+} during epidotization involving an oxidizing fluid phase. The fluid phase may also have sustained fluctuating Fe-compositions, since the single crystals of epidote in cavities exhibit irregular Fe–Al zoning (see Table 3). Garnet–epidote and clinopyroxene–epidote pairs are regarded to be in disequilibrium.

From a consideration of the data of Gustafson (1974), it is likely that in an approximately isothermal temperature regime, the original endoskarn assemblage of andradite–grossular garnet and diopside–hedenbergite pyroxene represents formation at lower f_{O_2} than the andradite exoskarn.

Trace elements. Trace element data for these endoskarn minerals are shown in Table 1, and their chondrite-normalized rare earth concentrations

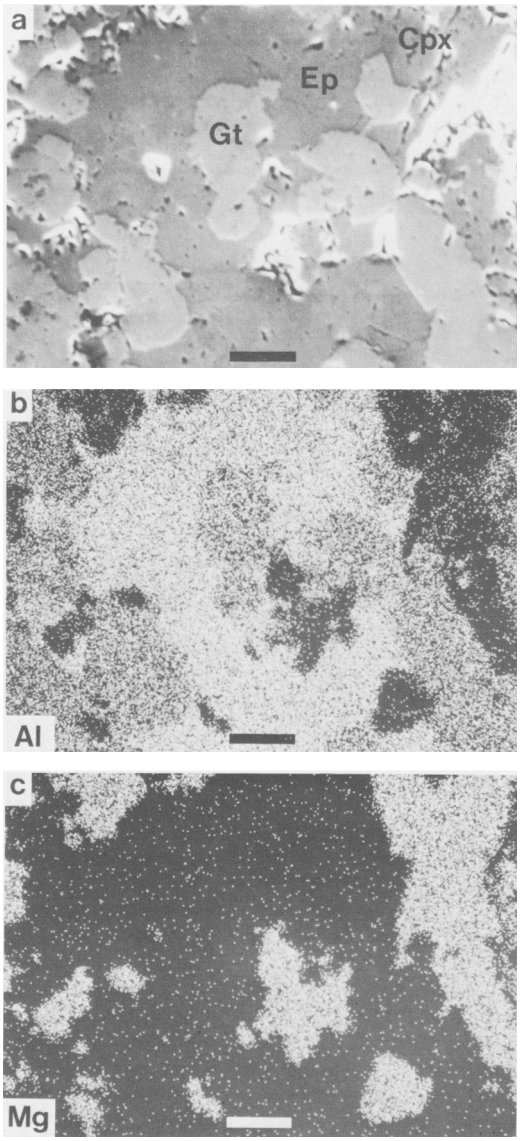

FIG. 5. Andradite–grossular garnet (Gt) and clinopyroxene (Cpx) intergrowth from endoskarn zone, showing extensive replacement of diopsidic clinopyroxene by epidote (Ep). (*a*) Backscattered scanning electron image; (*b*) Al X-ray map; (*c*) Mg X-ray map. Scale bar 30 μm.

are shown in Fig. 6. In general the chondrite-normalized *REE* patterns of the endoskarn minerals are less *LREE* enriched than the exoskarn minerals, and clearly do not have such marked negative Ce anomalies as the exoskarn minerals. This difference is likely to be the result of *REE* characteristics largely inherited from the different precursor materials of the exoskarn and endoskarn. The slightly negative Ce anomalies shown by the endoskarn minerals could have originated from the incorporation of a small *REE* component mobilized from the carbonate or exoskarn zone, especially if fluoro-complexes were formed in the fluid. However, in the case of the epidote (from cavities) with no Eu anomaly, a slightly negative Ce anomaly would also be consistent with an oxidizing environment. The epidote mineral separates are characterized by three distinct chondrite-normalized rare earth signatures: (1) epidote pseudomorphs after feldspar have a positive Eu anomaly, $(Eu/Eu^*)_{CN} = 1.39$, and are otherwise approximately linearly *LREE* enriched, $(La/Yb)_{CN} = 8.14$; (2) epidote replacing clinopyroxene has a negative Eu anomaly, $(Eu/Eu^*)_{CN} = 0.78$, and is otherwise approximately linearly *LREE* enriched, $(La/Yb)_{CN} = 6.17$; and (3) epidote from cavities has no Eu anomaly and is characterized by two ranges of approximate linearity with a pivot point about Gd, $(La/Sm)_{CN} = 2.15$ and $(Gd/Lu)_{CN} = 1.22$. Since plagioclase and K-feldspars commonly have positive Eu anomalies (e.g. Schnetzler and Philpotts, 1970; Drake, 1975), the positive Eu anomaly of epidote which has replaced feldspar is interpreted as having been inherited partially from original feldspars which preferentially partitioned Eu^{2+} into their structures. The rare earth signature and negative Eu anomaly characteristic of epidote replacing clinopyroxene are regarded as having been inherited largely from the clinopyroxene, since the rare earth

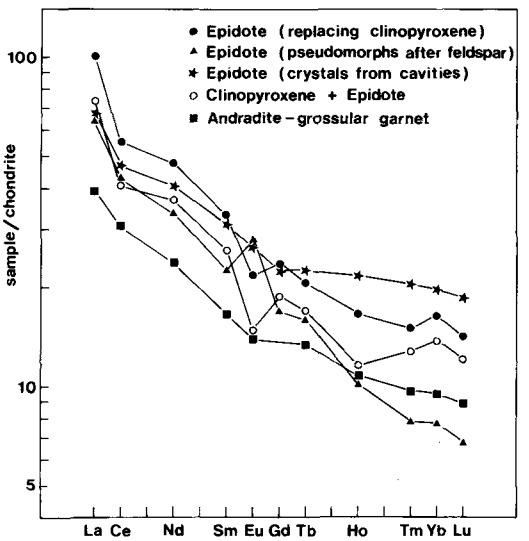

FIG. 6. Chondrite-normalized rare earth concentrations of endoskarn mineral separates. Data by INAA.

TABLE 3. MICROPROBE ANALYSES OF EPIDOTES, CLINOPYROXENES & GARNETS

Specimen no.	AR531								AR524							
	Wavelength dispersive analyses at 20 kV								Energy dispersive analyses at 15 kV							
	Epidotized volcanic breccia fragment in agglomerate		Epidote replacing clinopyroxene in intergrowth with garnet (see fig. 5)						Epidote replacing Clinopyroxene				Epidote single crystals in cavities. Irregular zoning.					
	Epidote pseudomorphs after feldspar		Epidote replacing clinopyroxene		Clinopyroxene		Andradite-grossular garnet		Epidote		Clinopyroxene		Zoned Epidote					
n=number of analyses	mean n=5	std. dev.	mean n=6	std. dev.	mean n=4	std. dev.	mean n=4	std. dev.	mean n=4	std. dev.	mean n=6	std. dev.	mean n=7	std. dev.	mean n=5	std. dev.	mean n=3	std. dev.
SiO_2	38.07	(0.41)	37.46	(0.44)	53.20	(0.33)	37.82	(0.20)	37.16	(0.72)	51.67	(0.24)	37.57	(0.31)	37.14	(0.42)	36.91	(0.23)
Al_2O_3	24.71	(0.40)	23.16	(0.70)	0.43	(0.17)	11.84	(0.36)	21.76	(0.88)	0.90	(0.44)	24.95	(0.49)	23.64	(0.39)	21.52	(0.75)
TiO_2	0.17	(0.10)	0.09	(0.05)	0.02	(0.02)	0.14	(0.11)	n.d.		n.d.		0.25	(0.45)	0.18	(0.24)	0.11	(0.18)
Cr_2O_3	0.01	(0.01)	0.01	(0.01)	0.01	(0.01)	0.02	(0.02)	n.d.		0.06	(0.15)	n.d.		n.d.		n.d.	
Fe_2O_3	11.38	(0.56)	12.92	(0.83)	-		14.94		15.77	(0.53)	-		11.93	(0.60)	13.35	(0.52)	16.35	(0.76)
FeO	-		-		8.68	(0.86)	0.43		-		11.96	(1.25)	-		-		-	
MgO	0.21	(0.17)	0.05	(0.03)	12.77	(0.55)	0.02	(0.02)	0.07	(0.13)	10.23	(0.64)	n.d.		n.d.		n.d.	
MnO	0.15	(0.18)	0.09	(0.06)	0.51	(0.07)	0.52	(0.07)	n.d.		0.49	(0.31)	n.d.		n.d.		n.d.	
CaO	23.71	(0.34)	23.45	(0.15)	25.06	(0.32)	34.63	(0.25)	23.28	(0.43)	24.15	(0.29)	23.83	(0.18)	23.57	(0.46)	23.27	(0.14)
H_2O (calc)	[1.90]		[1.87]		-		-		[1.87]		-		[1.90]		[1.88]		[1.86]	
total	100.31		99.10		100.68		100.36		99.91		99.46		100.43		99.76		100.02	
	(1)		(1)		(2)		(3)		(1)		(2)		(1)		(1)		(1)	
Si	2.997	3.000	3.004		1.985	2.000	2.994	3.000	2.985	3.000	1.981	2.000	2.961	3.000	2.964	3.000	2.969	3.000
Al^{IV}	0.003		-		0.015		0.006		0.015		0.019		0.039		0.036		0.031	
Al^{VI}	2.289		2.189		0.004		1.099		2.044		0.022		2.278		2.187		2.009	
Ti	0.010		0.005		0.001		0.008	1.998	-		-		0.015		0.011		0.006	
Cr	0.001		0.001		-		0.001		-		0.002		-		-		-	
Fe^{3+}	0.674	3.009	0.780	2.987	-	1.002	0.890		0.953	3.006	-	1.007	0.707	3.000	0.801	2.999	0.990	3.005
Fe^{2+}	-		-		0.271		0.028		-		0.383		-		-		-	
Mg	0.025		0.006		0.710		0.002		0.009		0.584		-		-		-	
Mn	0.010		0.006		0.016		0.035	3.002	-		0.016		-		-		-	
Ca	2.000		2.015		1.002		2.937		2.003		0.992		2.012		2.014		2.005	
OH	[1.000]		[1.000]		-		-		[1.000]		-		[1.000]		[1.000]		[1.000]	
$X_{Fe^{3+}}$(ep)	0.22 (0.01)		0.26 (0.02)						0.32 (0.02)				0.24 (0.01)		0.27 (0.01)		0.33 (0.02)	
Di-Hd					$Di_{72}Hd_{28}$ (3)						$Di_{60}Hd_{40}$ (4)							
$X_{Fe^{3+}}$(gt)							0.45 (0.02)											
corresponding activation analysis no.	1083						1086 (gt>>cpx,ep)		8315		8317 (cpx>ep)		8314					

n.d. = not detected by microprobe analysis.
(1) Epidote analyses converted to no. of ions on the basis of 12.5 O in the anhydrous state. Calculated ΣH_2O inserted on the assumption of one (OH) per formula unit, of the type $Ca_2(Al,Fe^{3+})_3Si_3O_{12}(OH)$. All Fe is assumed to be present as Fe^{3+}. $X_{Fe^{3+}}(ep) = Fe^{3+}/\Sigma$ octahedrally assigned cations.
(2) Clinopyroxene analyses presented as cations per 6 O. All Fe assumed to be present as Fe^{2+}.
(3) Garnet analysis presented as cations per 12 O. Fe_2O_3 and FeO calculated assuming stoichiometry of 8 cations and 12 O per formula unit. $X_{Fe^{3+}}(gt) = Fe^{3+}/\Sigma$ octahedrally assigned cations.

signature of the clinopyroxene + epidote separate is very similar to that of the pure epidote separated from this mixture, except that the absolute rare earth contents are all higher in the epidote. If the epidote in cavities is taken to be more nearly representative of the fluid composition and the redox conditions during epidotization (i.e. high Eu^{3+}/Eu^{2+}) then the strong negative Eu anomaly apparently characteristic of the pure clinopyroxene has been partly cancelled by an increased contribution of Eu^{3+} from the fluid during epidotization. Changing redox conditions during different phases of epidote crystallization may have affected the magnitudes of the Eu anomalies in the epidotes.

As with the rare earth elements, Th and U levels in the epidote replacing clinopyroxene may have been inherited largely from the precursor pyroxene. In contrast, however, Co, Ni and Zn levels in the clinopyroxene + epidote separate show a marked decrease in the epidote separated from this mixture, indicating that these elements probably behaved similarly to Mg and were partitioned into the fluid during epidotization. Co, Ni and Zn appear originally to have partitioned preferentially into the clinopyroxene relative to the coexisting andradite–grossular garnet. There is some evidence for an increased concentration of Co, Ni and Zn in the later-stage fluids, from which laumontite, prehnite and sphalerite crystallized (see Table 1 and Fig. 1). Although not determined, Cu may have behaved similarly to Co, Ni and Zn since chalcopyrite also occurs with sphalerite in later-stage veins.

Al and the trace elements Sc, Cr, Ni, Hf, Ta, Sb, Th and U all increase from exoskarn garnet G3 to the andradite–grossular garnets of the endoskarn, indicating that these elements may at least partially originate from the agglomerate. Depletion of Co and Zn in the endoskarn garnets relative to the exoskarn garnet G3 can be explained partly by the preferential partition of these elements into co-crystallizing clinopyroxene in the endoskarn. Since Ni also appears to be partitioned preferentially into clinopyroxene relative to garnet, the unexpected lower Ni concentration in exoskarn garnet G3 relative to the endoskarn garnets could arise if Ni behaved similarly to Mg during the formation of G3 and was partitioned strongly into the fluid phase. In addition, element distributions in garnets could be affected by the presence of steep chemical potential gradients in the fluid caused by the preferential uptake of certain trace elements by magnetite in the zone between the exoskarn and endoskarn garnets.

Some mafic agglomerate fragments in the endoskarn are not epidotized, but have been altered to amphibole and chlorite. The chondrite-normalized *REE* signature of one such fragment is shown in Fig. 8. The slope of this *REE* pattern and the absence of a strong negative Ce anomaly is consistent with the *REE* characteristics of the other endoskarn minerals, which are a function of agglomerate–fluid interaction. In contrast to the chondrite-normalized *REE* signatures of exoskarn minerals, the endoskarn minerals are less *LREE* enriched and lack strong negative Ce anomalies. These differences are illustrated in Fig. 8.

Late-stage minerals

The endoskarn and agglomerate contain lenses and veins (up to 1 cm wide) in which zeolites and calcite have crystallized interstitially to subhedral and euhedral quartz (see Fig. 7). Laumontite has been identified by X-ray diffractometry and microprobe analysis to be the main zeolite present. Small amounts of chabazite and an orange-coloured hydrous Mg-rich phase (zeolite?) are also present. Microprobe analyses of laumontite in these veins are given in Table 4. A complex intergrowth of both Ca-laumontite and K-rich laumontite ($K/(K+Ca+Na) = 0.64$) occurs interstitially to quartz. Whether this intergrowth is due to immiscible crystallization or to different stages of zeolite formation has not yet been established. It is apparent from the microprobe analyses that, within the zeolite structural framework, substitutions of the type 2K for Ca and KSi for CaAl are important. Na contents are generally low to insignificant. The K-rich phase also appears to contain less water and can be regarded as leonhardite, a partially dehydrated variety of laumontite. It is interesting to note that only the K-rich phase shows water deficiency. Sands and Drever (1978) have described

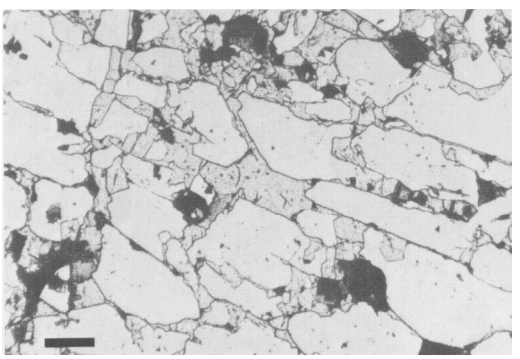

FIG. 7. Subhedral quartz with interstitial K-rich laumontite from a lens within the endoskarn, showing some evidence of distrubance of growth boundaries between quartz crystals before the crystallization of zeolite. Polished section, reflected light. Scale bar 100 μm.

TABLE 4. MICROPROBE ANALYSES OF PREHNITE AND ZEOLITES

	Energy dispersive analyses at 15 kV					
Specimen no.	AR540		AR524			
	Prehnite from fractures in exoskarn zone		Zeolites interstitial to subhedral quartz; lenses within endoskarn (see fig.7)			
	Prehnite		Laumontite		K-leonhardite	
n=number of analyses	mean n=6	std. dev.	mean n=6	std. dev.	mean n=6	std. dev.
SiO_2	42.80	(0.54)	52.66	(0.63)	51.97	(1.06)
Al_2O_3	22.00	(1.28)	20.16	(0.42)	18.01	(0.37)
Fe_2O_3	3.11	(1.94)	n.d.		n.d.	
MgO	0.04	(0.10)	n.d.		n.d.	
MnO	0.11	(0.17)	n.d.		n.d.	
Na_2O	0.12	(0.19)	n.d.		1.33	(0.24)
CaO	26.46	(0.31)	10.90	(0.43)	4.82	(0.33)
K_2O	n.d.		0.84	(0.26)	10.72	(0.82)
H_2O (calc)	[4.27]		[15.44]	(1.00)	[13.15]	(1.31)
total	98.91		100.00		100.00	
	(1)		(2)		(2)	
Si	3.006		16.50	23.94	16.74	23.57
Al^{IV}	-		7.44		6.83	
Al	1.821					
Fe^{3+}	0.164	1.996	-		-	
Mg	0.004		-		-	
Mn	0.007		-		-	
Na	0.016		-		0.83	
Ca	1.991	2.007	3.67	4.01	1.66	6.89
K	-		0.34		4.40	
OH	[2.000]		-		-	
H_2O	-		16.14		14.12	
$X_{Fe^{3+}}$(preh)	0.08 (0.05)					
X_K(zeo)			0.08 (0.03)		0.64 (0.02)	
corresponding activation analysis no.	8313		8318 (zeolites + quartz)			

n.d. = not detected by microprobe analysis.
(1) Prehnite analysis converted to no. of ions on basis of 11 O in the anhydrous state. Calculated %H_2O inserted on the assumption of $(OH)_2$ per formula unit, of the type $Ca_2(Al,Fe^{3+})_2Si_3O_{10}(OH)_2$. All Fe assumed to be present as Fe^{3+}. $X_{Fe^{3+}}$(preh) = $Fe^{3+}/(Fe^{3+} + Al)$.
(2) Zeolite analyses presented as cations and molecular H_2O per 48 O. Wt% H_2O calculated by difference from 100%. Theoretical laumontite $Ca_4(Al_8Si_{16})O_{48}.16H_2O$; theoretical leonhardite $Ca_4(Al_8Si_{16})O_{48}.14H_2O$ Substitutions $2K \leftrightarrows Ca$ and $KSi \leftrightarrows CaAl$ are apparent.
X_K(zeo) = K/(K+Ca+Na)

authigenic laumontite from deep-sea sediments with 4 wt. % K_2O ($K/(K+Ca) = 0.35$) as being considerably richer in potassium than laumontite from low-grade metamorphic terrains. However, no record has been found in the literature of laumontite as rich in potassium as that described here ($K/(K+Ca+Na) = 0.64$).

Prehnite also occurs in late-stage veinlets and microprobe analyses (Table 4) suggest that a variation of 2 to 14 atom % substitution of Al by Fe^{3+} is tolerated.

Trace elements. Trace element data for the laumontite + quartz and prehnite separates are shown in Table 1 and chondrite-normalized *REE* data are plotted in Fig. 8. Activation analyses of samples of laumontite with progressively higher proportions of quartz (coarser sieve fractions) show the same trace element characteristics, but with progressively lower trace element concentrations, indicating that these elements are accommodated predominantly in the zeolite phase. Semi-quantitative atomic absorption analysis of the laumontite + quartz separate gives a bulk ratio of $K/(K+Ca) = 0.2$. Calculations based on this ratio and the observed zeolite microprobe compositions indicate that the proportion of Ca-laumontite to K-laumontite (leonhardite) is about 2:1. In mixtures, these zeolites could not be distinguished satisfactorily by X-ray diffractometry. Co, Ni and Zn levels in these late-stage zeolites and prehnite are significant and, as already discussed, may be due to the concentration of these elements into the fluid phase during epidotization of clinopyroxene. Zn is especially concentrated by the zeolites. Only the zeolites contain significant levels of Rb and Cs, reflecting the ability of the zeolite structure to

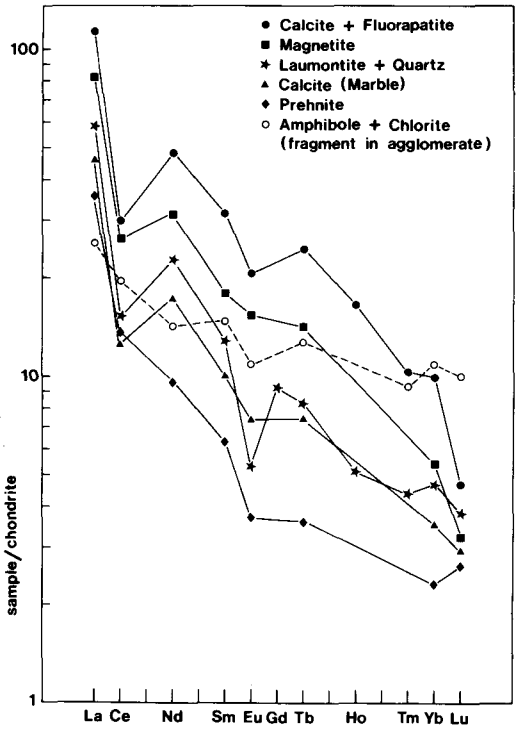

FIG. 8. Chondrite-normalized INAA rare earth data for the exoskarn minerals calcite, magnetite and fluorapatite. Laumontite and prehnite are late-stage vein minerals and have *REE* signatures similar to the marble. The amphibole + chlorite agglomerate fragment from the endoskarn zone has a less *LREE* enriched pattern consistent with other endoskarn minerals (see Fig. 6).

accommodate such large cations. In addition, Ta is taken up by the zeolites more strongly than by any of the other skarn minerals.

Chondrite-normalized rare earth plots for the laumontite + quartz and prehnite samples show strong *LREE* enrichment which is probably largely a function of the fluid composition. Similarities between the laumontite and marble *REE* patterns suggest that the fluid from which the laumontite crystallized was responsible for the coherent mobilization of *REE* from the marble. An increase in the fluorine content of the late-stage fluid may have been responsible for increased *REE* mobility, owing to an increase in fluoro-complex formation. The strong negative Eu anomaly in the laumontite signature probably reflects the reducing nature of this fluid. As in the case of garnet G3, the presence of both negative Ce and negative Eu anomalies in the laumontite does not necessarily provide conflicting evidence of redox conditions if the Ce is regarded as having been inherited from the already Ce-depleted marble, as discussed earlier.

Together, the presence of prehnite and zeolites indicates that the late-stage metasomatism involved a fluid rich in Al, Si and alkalis. The potassium could have been concentrated in the fluid phase as a result of the epidotization of K-feldspar.

Summary and conclusions

The earliest metasomatic fluid which reacted with the chalk Ca-source was probably rich in Mg, Fe and Si but poor in Al, and was of sufficiently low f_{O_2} and at a high enough temperature to allow diopside–hedenbergite pyroxene and wollastonite exoskarn to form. A change in the physicochemical conditions, however, resulted in the formation of the andradite exoskarn by almost total replacement of the early clinopyroxene. It is likely that a change to higher μ_{Fe} values and higher f_{O_2} in the fluid promoted the formation of andradite. In addition, the presence of fluorine in the fluid at this stage has been established from the presence of a fluor-hydrogarnet component in the exoskarn andradites and by the occurrence of fluorapatite in the marble.

The observed petrogenetic relationships between different phases of fluor-hydrogarnet formation in the exoskarn have enabled trends in fluid composition, oxidation state and trace element redistribution as a function of time to be elucidated. Exoskarn garnet compositions indicate an evolutionary trend of increasing μ_{Al}/μ_{Fe} in the fluid, decreasing f_{O_2}, decreasing temperature, increasing trace element uptake and increasing *HREE* fractionation by garnet during *REE* redistribution. In the exoskarn, fluorapatite and magnetite preferentially partition all *REE* relative to calcite and the early-formed garnets. The *REE* patterns of the exoskarn minerals, including the negative Ce anomalies are interpreted as having been inherited largely from the marble. Individual *REE* signatures with both negative Ce and negative Eu anomalies are therefore regarded as the result of successive processes probably involving (*a*) the original removal of Ce^{4+} from seawater in an oxidizing environment before the formation of the chalk, and (*b*) the crystallization/recrystallization of the exoskarn under more reducing conditions. The presence of fluorine in the metasomatic fluid is thought to have contributed to the local mobility and fractionation of *REE*.

The major and trace element compositions of the endoskarn garnets, clinopyroxenes and epidotes are thought to reflect the chemical composition of the precursor agglomerate, modified by fluid–rock interaction. The *REE* patterns of endoskarn

minerals are less *LREE* enriched than the exoskarn minerals which replaced the carbonate. The epidotization of the endoskarn is thought to have taken place under more oxidizing conditions than the original garnet–clinopyroxene endoskarn formation. Epidote which has replaced feldspars has a positive Eu anomaly which is regarded to have been partially inherited from the feldspar. In contrast, epidote which has replaced clinopyroxene appears partially to have inherited a negative Eu anomaly from the clinopyroxene. Epidote which crystallized from the fluid in cavities has no Eu anomaly.

The late-stage minerals, laumontite and prehnite, indicate a trend towards increased μ_{Al}/μ_{Fe} and μ_K/μ_{Ca} in the fluid with time, and the concentration of Co, Ni and Zn in the late-stage fluids. The *REE* pattern of laumontite indicates that there was probably an increase in the mobilization of *REE* from the marble during the late-stage metasomatism. This could be related to an increase in the fluorine content of the fluid.

The compositions of the Ca-rich skarn minerals, produced as a result of fluid-limestone xenolith interaction in this volcanic caldera, have preserved a record of the effects of changing physicochemical conditions during their formation. An attempt has therefore been made to elucidate the nature of element distribution behaviour, fluid evolution characteristics and skarn formation conditions as a function of time, from mineral compositions and their petrogenetic relationships.

Skarn minerals in general, and garnets in particular, often exhibit complex compositional variations. If distinctions between different episodes of mineral growth can be recognized and separately analysed, then this approach may be of use in elucidating skarn rock–fluid interaction histories.

Acknowledgements

I wish to thank colleagues in the Department of Mineralogy, British Museum (Natural History) for their help with this work, particularly Dr C. T. Williams who carried out the INAA analyses, V. K. Din who determined the water and fluorine contents and iron oxidation states in the garnets, E. E. Fejer and J. G. Francis who carried out the garnet cell-edge determinations and Drs A. C. Bishop, P. Henderson and C. T. Williams for helpful discussions and their comments on the manuscript. I also thank Dr F. B. Atkins, Department of Earth Sciences, University of Oxford, for helpful comments.

References

Abbey, S. (1983) *Geol. Surv. Can. Paper* no. 83-15.

Alderton, D. H. M., Pearce, J. A., and Potts, P. J. (1980) *Earth Planet. Sci. Lett.* **49,** 149–65.

Apted, M. J. and Boettcher, A. L. (1981) *Geochim. Cosmochim. Acta* **45,** 827–37.

Atkinson, W. W. Jr., Kaczmarowski, J. H., and Erickson, A. J. Jr. (1982) *Econ. Geol.* **77,** 899–918.

Burt, D. M. (1974) In *Geochemical transport and kinetics* (A. W. Hofmann *et al.*, eds.), 287–93.

Din, V. K. and Jones, G. C. (1978) *Chem. Geol.* **23,** 347–52.

Drake, M. J. (1975) *Geochim. Cosmochim. Acta* **39,** 55–64.

Einaudi, M. T. and Burt, D. M. (1982) *Econ. Geol.* **77,** 745–54.

—— Meinert, L. D., and Newberry, R. J. (1981) Ibid. 75th Ann. Vol., 317–91.

Fleet, A. J. (1984) In *Rare earth element geochemistry* (P. Henderson, ed.), 343–73.

Gordon, T. M. and Greenwood, H. J. (1971) *Am. Mineral.* **56,** 1674–88.

Greenwood, H. J. (1967) Ibid. **52,** 1669–80.

Gunn, W. (1903) *Mem. Geol. Surv. Scotl.* 200 pp.

Gustafson, W. I. (1974) *J. Petrol.* **15,** 455–96.

Harris, N. B. and Einaudi, M. T. (1982) *Econ. Geol.* **77,** 877–98.

Henderson, P. and Williams, C. T. (1981) *J. Radioanal. Chem.* **67,** 445–52.

Irving, A. J. (1978) *Geochim. Cosmochim. Acta* **42,** 743–770.

—— and Frey, F. A. Ibid. **42,** 771–85.

King, B. C. (1954) *Trans. Geol. Soc. Glasgow* **21,** 440–6.

——(1955) *Q. J. Geol. Soc. Lond.* **110,** 323–55.

Kitamura, K. (1975) *Econ. Geol.* **70,** 725–38.

McKerrow, W. S. and Atkins, F. B. (1985) *Geol. Assoc. Guide*, Isle of Arran.

Novak, G. A. and Gibbs, G. V. (1971) *Am. Mineral.* **56,** 791–825.

Pride, C., and Muecke, G. K. (1981) *Contrib. Mineral. Petrol.* **76,** 463–71.

Sands, C. D. and Drever, J. I. (1978) In *Natural zeolites, occurrence, properties, use.* (L. B. Sand and F. A. Mumpton, eds.), 269–75.

Schnetzler, C. C. and Philpotts, J. A. (1970) *Geochim. Cosmochim. Acta* **34,** 331–40.

Shimazaki, H. (1969) *J. Fac. Sci. Univ. Tokyo* sect. 2, **17,** 317–50.

Shoji, T. (1974) *J. Mineral. Soc. Japan* **11,** 359–72.

——(1975) *Econ. Geol.* **70,** 739–49.

Sigurdsson, H. (1977) *J. Volc. Geoth. Res.* **2,** 165–86.

Taylor, B. E. and Liou, J. G. (1978) *Am. Mineral.* **63,** 378–93.

Tyrrell, G. W. (1928) *Mem. Geol. Surv. Scotl.* 292 pp.

Uchida, E. and Iiyama, J. T. (1982) *Econ. Geol.* **77,** 809–22.

Wakita, H., Rey, P., and Schmitt, R. A. (1971) *Proc. 2nd Lunar Sci. Conf.* 1319–29.

Walker, G. P. L. (1971) in *Studies in Earth Sciences, West Commemoration Vol.* (T. V. V. G. R. K. Murty and S. S. Rao, eds.), 181–94.

Williams, H. and McBirney, A. R. (1979) *Volcanology*, 397 pp.

[*Manuscript received 12 May 1986*]